Charge Localization in Defective BiVO<inf>4</inf>

(article starts on next page)

Article

Charge Localization in Defective BiVO$_4$

Nicklas Österbacka, Francesco Ambrosio, and Julia Wiktor*

Read Online

ACCESS | Metrics & More | Article Recommendations | Supporting Information

ABSTRACT: We study the native defects in bismuth vanadate using hybrid density functional theory. We pay special attention to where excess charges localize by considering different polaronic distortions and find that charge localization has a profound effect on the local chemical environment around certain defects. In particular, oxygen dimerization may occur in the presence of acceptor defects. On the basis of Fermi level pinning due to compensation between donors and acceptors we additionally find that intrinsic p-type conductivity is difficult to achieve in BiVO$_4$, in good agreement with experimental observations. Our results give new insights into the defect chemistry of bismuth vanadate and act as a guide for future studies on defects in complex metal oxides.
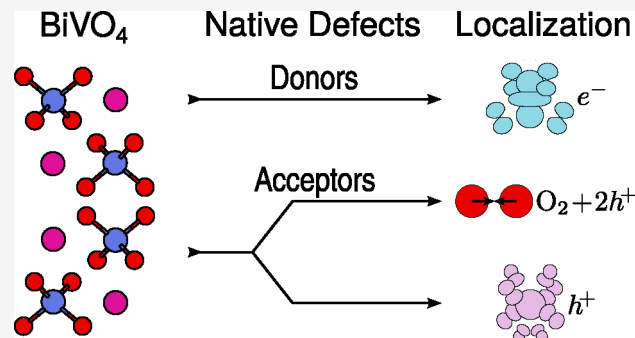
INTRODUCTION

Large parts of our society are currently transitioning away from fossil fuels and pivoting toward more sustainable energy sources. Photo-electrocatalytic (PEC) water splitting, the production of hydrogen gas from water through solar irradiation, could become a promising alternative source of clean and sustainable fuel. In this context, large efforts have been put into the investigation of potential materials that could be used as catalysts.[1,2] However, many promising candidates are still marred by problems such as insufficient efficiency, poor reaction kinetics, and unacceptable degradation over time.[3,4] These issues must be overcome in order for PEC water splitting to become a solid pillar of the energy economy, and their solution requires an improved understanding of the relationship between the structure and functionality of these materials. The monoclinic scheelite phase of bismuth vanadate, BiVO$_4$, is one of the most promising materials for facilitating PEC water splitting due to its favorable band alignment with the water oxidation potential and moderate band gap of ∼2.4 eV.[5] As a consequence, it has been the subject of extensive research during the past decade and has been proposed as a good platform for understanding mechanisms in other complex transition-metal oxides.[6] Despite its valuable properties, the PEC efficiency of BiVO$_4$ is still limited by a high charge recombination rate, low conductivity, and slow hole transfer.[5] Much experimental effort has been put toward circumventing or solving these issues through synthesis and postsynthesis procedures.[7−13] In fact, synthesis conditions directly affect the concentration and nature of defects within the material, while postsynthetic treatments can modify the defect chemistry of the material.[14] Within this framework, understanding the energetics and the defect chemistry of native defects in BiVO$_4$ can aid in the endeavor of improving its PEC efficiency.

However, unravelling their effects through experiments is often nontrivial.

Among the native defects, oxygen vacancies have been studied most extensively. Their abundance has been reported to increase the majority charge carrier conductivity[15] as well as the overall PEC efficiency of bismuth vanadate.[16,17] Their role is not entirely without controversy, however, as they have also been reported to be detrimental to the charge-transfer properties of the material.[18] Unfortunately, the experimental literature is sparser concerning the effects of the other native defects. Similarly, theoretical papers have mainly focused on oxygen vacancies,[19−21] though studies on the other defects have been published. In particular, Yin et al.[22] and Zhang et al.[23] presented formation energies calculated using density functional theory (DFT). The former used a semilocal exchange-correlation functional for both geometry relaxation and total energy calculations. The latter performed total energy calculations using DFT+U and hybrid DFT, based on the geometries found at the semilocal level of theory. Both studies predict a strong p-type conductivity for samples synthesized in oxygen-rich conditions, a finding that is in stark contrast with experimental measurements indicating that BiVO$_4$ is an n-type semiconductor.[5] While examples of undoped p-type BiVO$_4$ are documented in the literature[24,25] the extreme p-type character predicted by Yin et al. and Zhang et al. indicates that it should be far more prevalent. Cooper et al. highlight this discrepancy
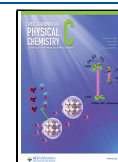
between theory and experiment and suggest that hydrogen impurities may play a key role in the n-type conductivity generally observed in $BiVO_4$ samples.[26] However, this was based on the prediction by Yin et al., whose calculations fail to take charge localization into account.

Excess charges are known to preferentially localize and form polarons in many transition-metal oxides including $BiVO_4$.[27−32] Semilocal exchange-correlation functionals fail to capture this phenomenon, tending to instead delocalize charges, due to electron self-interaction errors.[33,34] While Zhang et al. performed calculations using DFT+U and hybrid functionals, both of which can overcome this limitation,[33−36] the geometries of their atomistic models were optimized using a semilocal functional, which could lead to erroneous charge delocalization for some of the defects.

In this work, we study the native defects of $BiVO_4$ and calculate their formation energies, carefully taking polaronic distortions and charge localization into account through the use of hybrid density functionals. We show that this yields Fermi levels pinned at energies more in line with experiments than previous theoretical studies. In particular, we show that p-type conductivity is difficult to achieve. We focus on the geometry and charge localization of the defective structures and show that oxygen dimers tend to form for acceptor defects.

■ COMPUTATIONAL DETAILS

The calculations were performed using the Gaussian Plane Waves method of density functional theory as implemented in
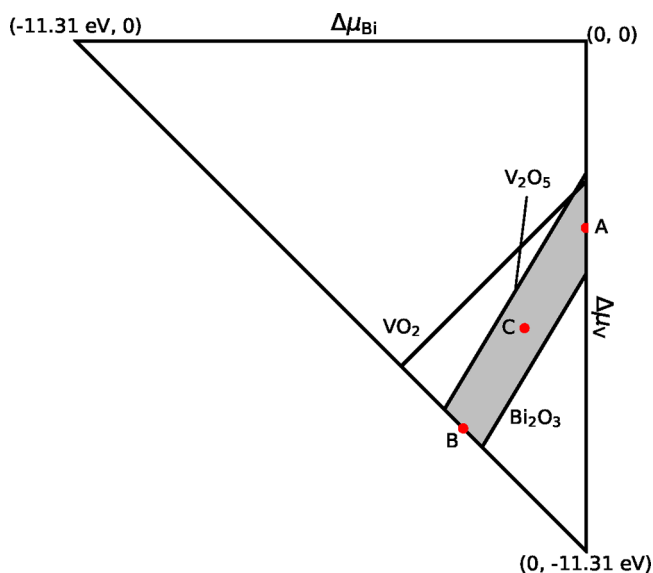

Figure 1. Phase diagram of $BiVO_4$ and competing phases. The shaded area represents the stability region of $BiVO_4$, i.e., where eqs 4−9 are fulfilled. The values (in eV) of $(\Delta\mu_{Bi}, \Delta\mu_V, \Delta\mu_O)$ at points A, B, and C are approximately $(0.0, -4.14, -1.79)$, $(-2.72, -8.59, 0)$, and $(-1.36, -6.37, -0.90)$, respectively.

the CP2K code.[37] Goedecker-Teter-Hutter pseudopotentials were used to describe core−valence interactions.[38] Wave functions were expanded using double-ζ polarized MOLOPT basis sets[39] along with an auxiliary plane-wave basis set defined up to an energy cutoff of 600 Ry. We employed the PBE0-TC-LRC exchange-correlation functional[40,41] with 22% exact exchange along with the auxiliary density matrix method[42] to

speed up calculations. The Brillouin zone was sampled at the Γ point.

We considered the monoclinic scheelite phase using a $2 \times 2 \times 2$ repetition of the experimental unit cell reported by Sleight et al.,[43] that is, a structure of space group $I2/b$ exhibiting lattice parameters of $a = 5.1935$ Å, $b = 5.0898$ Å, $c = 11.6972$ Å, and $\gamma = 90.387$, yielding a pristine supercell consisting of 192 atoms. We relaxed the atomic positions of all structures until the residual forces on all atoms were less than 10 meV/Å.

Formation Energies and Chemical Potentials. To assess the stability of various defects, we calculate their formation energies. The formation energy $E^f[X^q]$ of a defect of type X in charge state q may be expressed as[44]

$$E^f[X^q] = E[X^q] - E_0 - \sum_i \mu_i n_i + q(\varepsilon_v + \varepsilon_F) + E_{corr}$$

(1)

where $E[X^q]$ is the total energy of the supercell containing the defect, E_0 is the total energy of the pristine material, μ_i is the chemical potential of defect i, n_i is the number of defect atoms added of type i, ε_v is the location of the valence band maximum, ε_F is the Fermi energy, and E_{corr} is a correction term added to compensate for electrostatic interactions between periodic repetitions of the charged defect. To this end, we employ the correction scheme of Freysoldt, Neugebauer, and Van de Walle, neglecting the alignment factor.[45]

The chemical potentials of the constituent elements of $BiVO_4$ are subject to thermodynamic constraints, which may be used to model experimental growth conditions.[44] The growth of $BiVO_4$ under equilibrium conditions is subject to the constraint

$$\mu_{Bi} + \mu_V + 4\mu_O = E_{BiVO_4}$$

(2)

where μ_i is the chemical potential of the compound i. To directly include the choice of references for chemical potentials, the constraint is rewritten in terms of the formation energy $\Delta H_f(BiVO_4)$, which may be expressed as

$$\Delta H_f(BiVO_4) = E_{BiVO_4} - E_{Bi} - E_V - 4E_O$$

(3)

Here E_i is the total energy per formula unit of compound i. Bismuth and vanadium are referred to the pure metallic phase, while oxygen is referred to half of the energy of an isolated oxygen molecule. Combining eqs 2 and 3 and rearranging yields

$$\Delta H_f(BiVO_4) = (\mu_{Bi} - E_{Bi}) + (\mu_V - E_V) + 4(\mu_O - E_O)$$

(4)

$$= \Delta\mu_{Bi} + \Delta\mu_V + 4\Delta\mu_O$$

(5)

where $\Delta\mu_i = \mu_i - E_i$ is the chemical potential change of species i referenced to a pure phase specified above.

Additionally, the formation of bulk metal and gaseous oxygen must be prevented, limiting the chemical potentials to
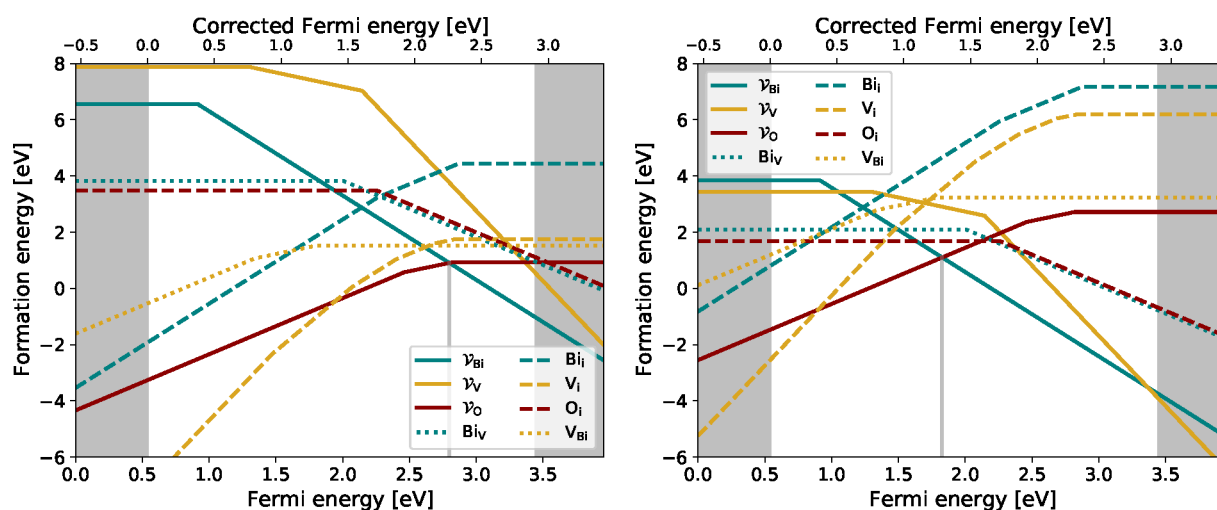
$$\Delta\mu_{Bi} \leq 0, \ \Delta\mu_V \leq 0, \ \Delta\mu_O \leq 0$$

(6)

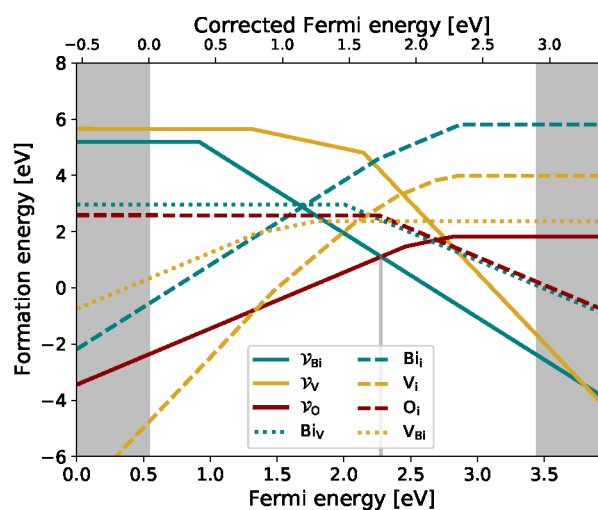To avoid the formation of secondary phases, we have the additional constraints

$$\Delta H_f(V_2O_5) \geq 2\Delta\mu_V + 5\Delta\mu_O$$

(7)

$$\Delta H_f(VO_2) \geq \Delta\mu_V + 2\Delta\mu_O$$

(8)

$$\Delta H_f(Bi_2O_3) \geq 2\Delta\mu_{Bi} + 3\Delta\mu_O$$

(9)

(a) Bismuth-rich/oxygen-poor condition (A).

(b) Oxygen-rich/bismuth-poor condition (B).

(c) Bismuth/oxygen-moderate condition (C).

Figure 2. Defect formation energies calculated according to eq 1 at different conditions. $\mathcal{V}_A$ denotes a vacancy on the site of an A atom, A_i denotes an interstitial A atom, and A_B denotes a substitutional A atom on a B site. Shading indicates band edge shifts due to spin−orbit coupling, thermalization, and nuclear quantum motion as previously calculated by Ambrosio et al.[46]

where formation energies are calculated analogously to eq 3. The resulting phase diagram is shown in Figure 1, where the shaded area represents the BiVO$_4$ region of stability taking the restrictions above into account.

The chemical potential calculations are based on experimental unit cells, with lattice parameters and space groups listed in Table S1 of the Supporting Information.

RESULTS

Defect Formation Energies. We first determine formation energies of various defects as a function of growth conditions by varying the chemical potentials of eq 1. A diagram of allowed chemical potentials is calculated according to the procedure described above and is presented in Figure 1. The labeled points indicate the conditions we calculate formation energies for: bismuth-rich/oxygen-poor conditions (A), oxygen-rich/bismuth-poor conditions (B), and bismuth/oxygen-moderate conditions at the midpoint between the former two (C).

Defect formation energies at the chosen conditions are plotted in Figure 2, and charge transition levels are shown in Figure 3, where the latter is defined as the Fermi level at which the formation energies of a particular defect in two different charge states are equal. We note that charge transition levels are independent of the chemical potentials. The calculated band gap is ∼3.95 eV, significantly larger than the experimental room-temperature value of ∼2.4 eV.[5] This discrepancy primarily stems from significant band gap renormalization and band-edge shifts that occur in BiVO$_4$ due to spin−orbit coupling, thermalization, and nuclear quantum motion that are not explicitly considered in our calculations. To account for this, we correct the band edges using values reported by Ambrosio et al.[46] The valence band maximum is shifted upward by 0.54 eV, and the conduction band minimum shifts downward by 0.51 eV, reducing the calculated band gap from 3.95 to 2.9 eV. This brings it into closer alignment with the experimental band gap of 2.4 eV. The corrected band edges are indicated by shading in Figures 2 and 3.
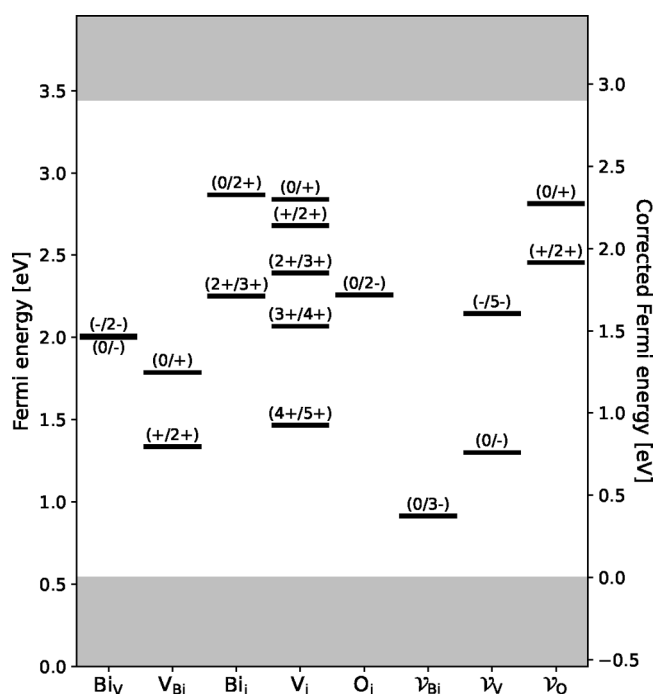
Figure 3. Defect charge transition levels. Shading indicates band edge shifts due to spin−orbit coupling, thermalization, and nuclear quantum motion as previously calculated by Ambrosio et al.[46]

(a) Neutral charge state.

(b) -1 charge state.

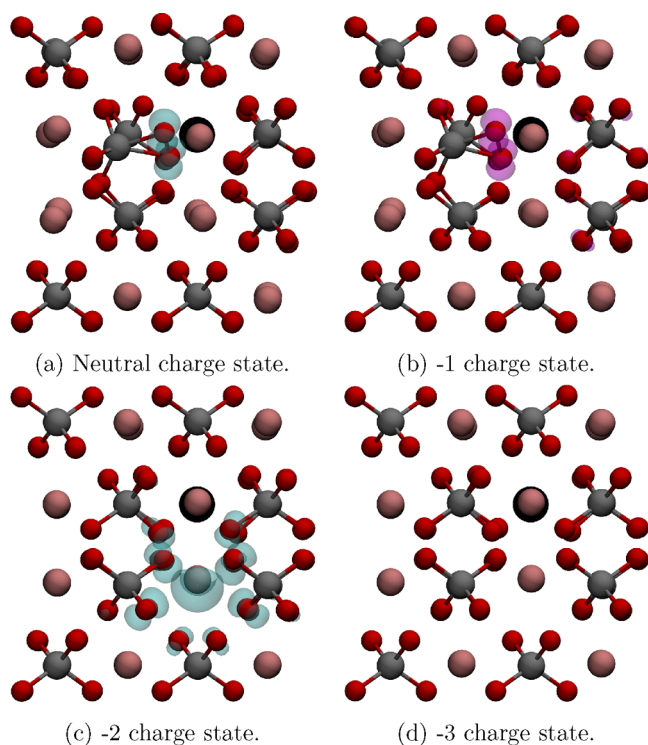(c) -2 charge state.

(d) -3 charge state.

Figure 4. Lowest-energy configurations for the bismuth vacancy. The approximate location of the removed atom is shown in black. Isosurfaces represent the square modulus of orbitals associated with localized charges and are shown at 5% of their maximum values. Holes are shown in cyan, and electron states related to dimer formation are shown in magenta.

The Fermi level is pinned at the lowest-energy intersection between donor and acceptor formation energies. This is marked by vertical lines in Figure 2. At this point, the

formation of further acceptor defects would be compensated by the formation of donors, and vice versa. For conditions A and C (see Figure 1) this phenomenon pins the Fermi level above the band gap middle, implying n-type conductivity, with oxygen vacancies as the dominant donor defect. The formation energy of oxygen vacancies at an oxygen-rich condition is in excellent agreement with the calculations of Seo et al.[47] For condition B, the Fermi level is pinned just below the band gap middle, implying a weak p-type conductivity with bismuth vacancies and oxygen interstitials being the dominant acceptor defects. Charge transition levels are plotted in Figure 3. Bi_i^+ is the only unstable electron donor, while $\mathcal{V}_{Bi}^-$, $\mathcal{V}_{Bi}^{2-}$, $\mathcal{V}_V^{2-}$, $\mathcal{V}_V^{3-}$, $\mathcal{V}_V^{4-}$, and O_i^- are unstable acceptors. Additionally, Bi_V^- is stable only for a Fermi energy range spanning less than 0.1 eV.

In the following, we inspect the considered defects in different charge states starting from the case with excess electrons and holes removed. We successively add the charges one by one until charge neutrality is reached, investigating how the charges localize and how defect geometries are affected.

Bismuth Vacancy. The bismuth vacancy acts as an electron acceptor, contributing three excess holes at charge neutrality. Its structure and charge localization at different charge states is shown in Figure 4. In the absence of excess charges, that is, at the −3 charge state, the vacancy induces slight lattice distortions immediately surrounding the defect. The eight closest oxygen atoms are pushed away by an average of ∼0.16 Å, and the four closest Bi atoms are pulled 0.2 Å closer to the vacant site. Adding one excess hole results in the formation of a polaron next to the defect, centered on a bismuth atom, similar to that previously observed in the pristine bulk.[31] The Bi−O bond lengths formed by the bismuth atom trapping the charge and the eight surrounding oxygen atoms are shortened by ∼0.03−0.1 Å. Upon the addition of a second hole, two oxygen atoms of a VO4 neighboring the vacancy are pushed together, forming a dimer onto which the two holes localize. The dimer has an O−O bond length of 1.44 Å, close to that of the O_2^{2-} species and in good agreement with previous observations for double-hole induced oxygen dimerization in pristine BiVO4[32] and other metal oxides.[48−50] It remains bound to its host vanadium with V−O bond lengths of 1.82 and 1.87 Å. The host vanadium is displaced from its pristine lattice position by 0.72 Å and forms a bond with an oxygen atom of a neighboring VO4. A third hole localizes onto the oxygen dimer, reducing its O−O bond length to 1.31 Å, consistent with what is expected for the O_2^{1-} species. Furthermore, the V−O bonds to the host vanadium are elongated to 1.92 and 1.95 Å.

The formation of the oxygen dimer pushes the state associated with its two holes far into the conduction band, where hybridization with cation states occurs.[48] For this reason, it is impossible to isolate these two holes for visualization. The oxygen dimerization is additionally associated with the localization of several electronic states similar to O2 molecular orbitals; for illustrative purposes, we thus use the highest-lying of these states in Figure 4b.

Vanadium Vacancy. Removing a vanadium atom frees up the four oxygen atoms coordinated to it and yields five excess holes under charge neutral conditions. Figure 5 shows the structure of the defect in different charge states as well as the location of excess charges. In the −5 charge state, the four oxygen atoms bind to two bismuth atoms each with Bi−O bond lengths of ∼2.1 Å. Neither the bismuth nor oxygen atoms

(a) Neutral charge state.   (b) -1 charge state.   (c) -2 charge state.

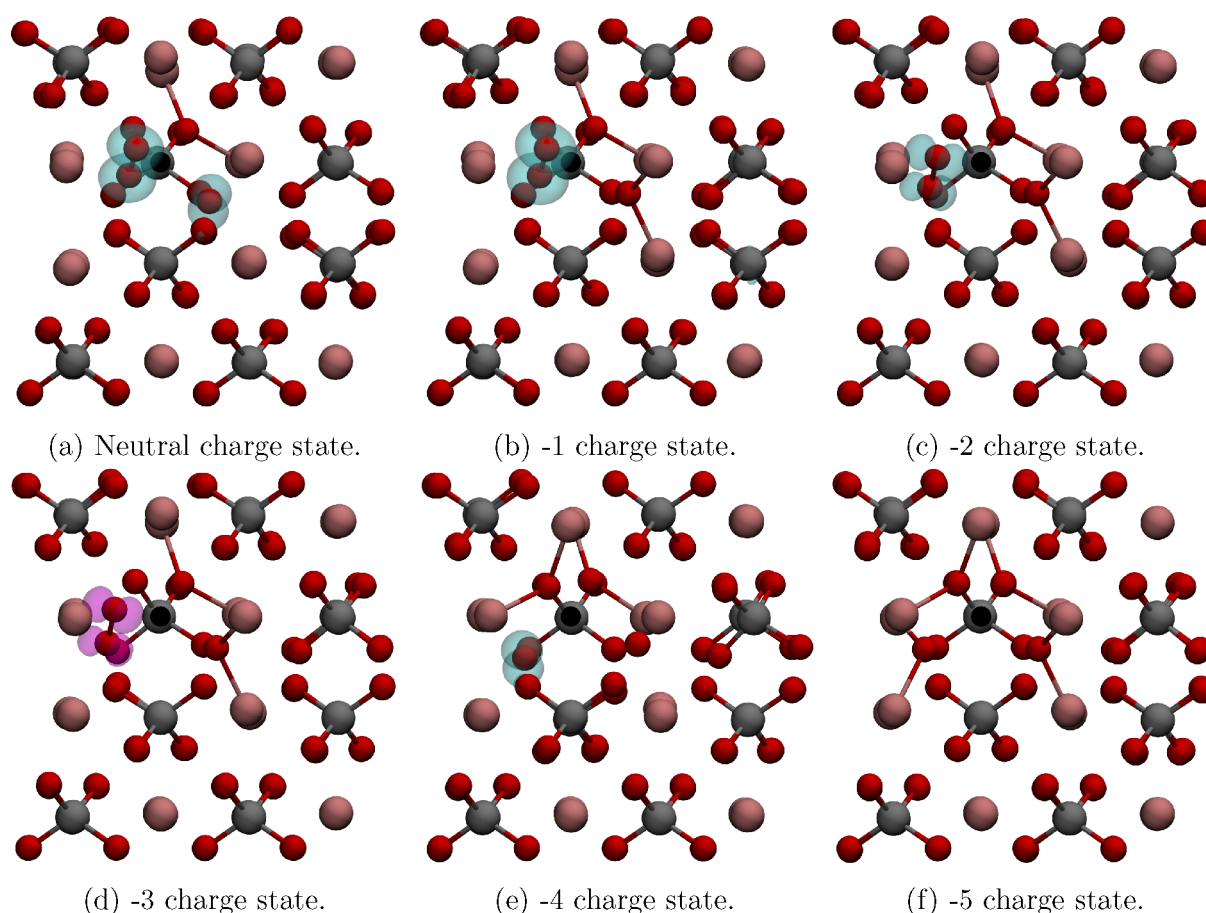(d) -3 charge state.   (e) -4 charge state.   (f) -5 charge state.

Figure 5. Stable configurations for the vanadium vacancy. The approximate location of the removed atom is shown in black. Isosurfaces represent the square modulus of orbitals associated with localized charges and are shown at 5% of their maximum values. Holes are shown in cyan, and electron states related to dimer formation are shown in magenta.
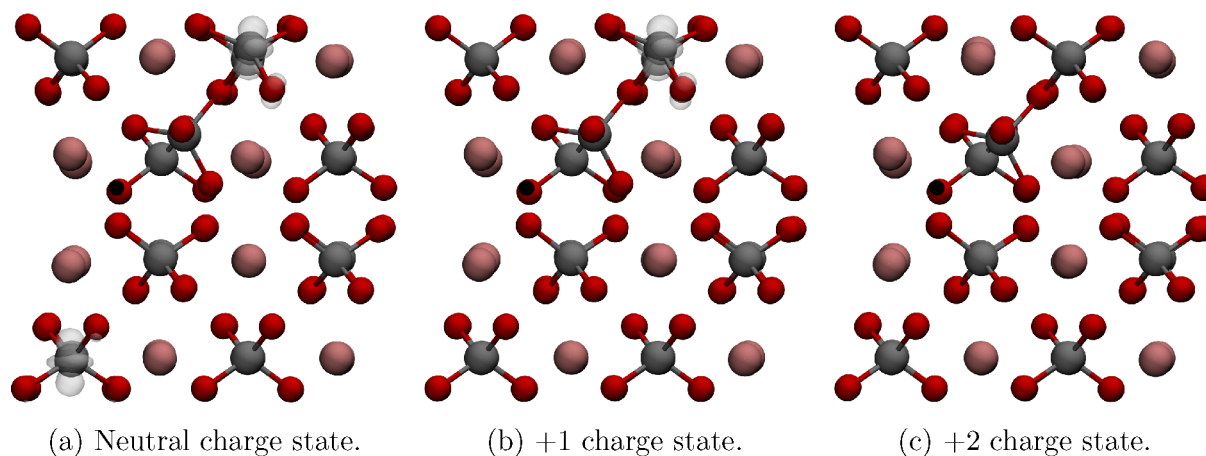

(a) Neutral charge state.   (b) +1 charge state.   (c) +2 charge state.

Figure 6. Lowest-energy configurations for the oxygen vacancy. The approximate location of the removed atom is shown in black. Isosurfaces represent the square modulus of orbitals associated with localized electrons and are shown at 5% of their maximum values.

deviate from their positions in the pristine lattice by more than 0.4 Å in this process. Localization occurs upon the addition of a hole, centered on one of the bismuth-bonded oxygen atoms. The associated Bi−O bonds elongate to ∼2.3 Å. Additionally, the Bi−O bonds of another bismuth-bonded oxygen atom increase to ∼2.2 Å. Adding a second hole causes the formation of an oxygen dimer with an O−O bond length of 1.44 Å, again in line with the O_2^{2-} species. Similarly, a third hole shortens the dimer O−O bond length to 1.3 Å, as in the O_2^{1-} species.

The addition of a fourth hole further reduces the dimer O−O bond to 1.2 Å, which is close to the bond length of the O_2 molecule. A fifth hole localizes onto one of the remaining bismuth-bonded oxygen atoms as observed for the −4 charge state.

The hole states associated with dimer formation are impossible to isolate due to hybridization, just like in the case of the bismuth vacancy above. Therefore, we again show
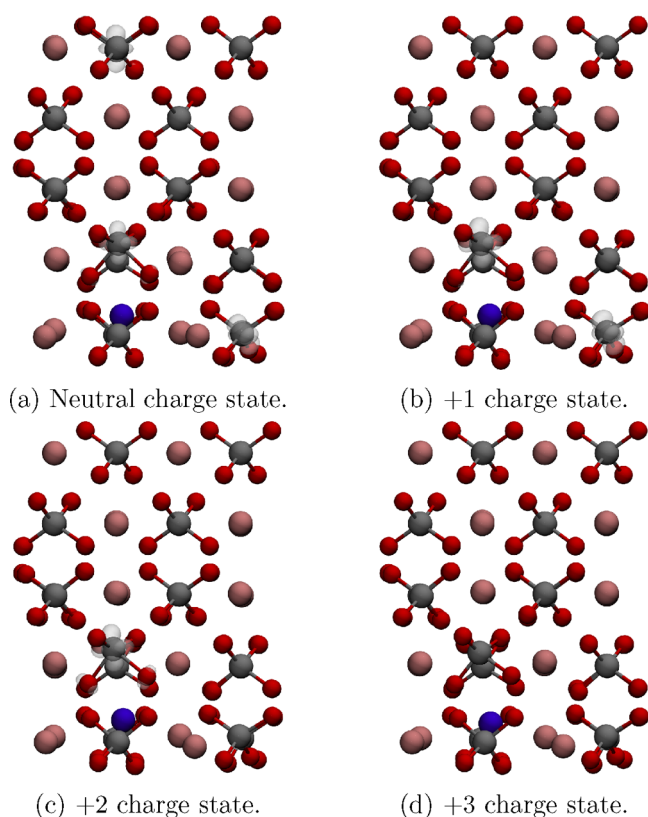
(a) Neutral charge state.   (b) +1 charge state.

(c) +2 charge state.   (d) +3 charge state.

Figure 7. Stable configurations for interstitial bismuth. The defect is highlighted in blue. Isosurfaces represent the square modulus of orbitals associated with localized electrons and are shown at 5% of their maximum values.

the highest-lying electron state associated with the dimer in Figure 5d.

Oxygen Vacancy. Oxygen vacancies in BiVO$_4$ are donors, contributing two electrons in the case of charge neutrality. The defect's structure, along with the localization of excess charges, is shown in Figure 6 for different charge states. When an oxygen vacancy is introduced, the undercoordinated vanadium atom ($V_{Vacancy}$) is found to move toward a neighboring VO$_4$ in order to form a bond with one of its oxygen atoms and regain its fourfold coordination. Without any excess charges, that is, in the +2 charge state, the $V_{Vacancy}$ atom is displaced from its pristine lattice position by 0.9 Å toward the vanadium atom it shares an oxygen with ($V_{Neighbor}$). The shared oxygen is pulled 0.3 Å closer to $V_{Vacancy}$, with a $V_{Vacancy}$−O bond length of 1.84 Å and a $V_{Neighbor}$−O bond length of 1.82 Å. The addition of an excess electron induces charge localization onto $V_{Neighbor}$ elongating the $V_{Neighbor}$−O bonds of the unshared oxygen atoms to ∼2 Å. A second excess electron forms a polaron on a VO$_4$ in the bulk region of the material, elongating its V−O bonds to ∼1.8 Å. The bridged structure remains unperturbed.

Interstitial Bismuth. The bismuth interstitial, a donor yielding three excess electrons in the neutral charge state, resides in between two bismuth atoms in the lattice, shifted slightly toward a VO$_4$ in a neighboring plane. The structure and charge localization of the defect in different charge states is shown in Figure 7. This defect causes significant displacements of the atoms in its immediate vicinity. In the +3 charge state, that is, without excess charges, the bismuth atoms surrounding the defect are pushed away, ending up between 0.2 and 0.8 Å from their positions in the pristine lattice. Most of the

surrounding vanadium atoms are displaced by up to 0.3 Å compared to their positions in the pristine lattice, though the vanadium lying above the interstitial in Figure 7d is pushed away by 0.64 Å and its V−O bonds are significantly distorted compared to the tetrahedral shape taken in the bulk. Localization onto the distorted VO$_4$ above the interstitial occurs upon the insertion of an excess electron, elongating the V−O bonds pointing away from the defect by less than 0.1 Å and the V−O bonds closest to the defect by ∼0.15 Å. Inserting a second electron results in the formation of a polaron on a VO$_4$ in close vicinity of the interstitial, causing its V−O bonds to elongate slightly. Two nearby bismuth atoms are also pulled ∼0.2 Å toward the localized charge. Adding a third electron forms another polaron on a VO$_4$ in the bulk-like region far away from the defect causing its V−O bonds to elongate by ∼0.8 Å as expected in the bulk of BiVO$_4$.[31]

Interstitial Vanadium. The vanadium interstitial acts as a donor, contributing five excess electrons in the charge neutral state. It preferentially resides in the void between two layers of the BiVO$_4$ structure and induces strong lattice deformations in its neighborhood, giving rise to a complex bond arrangement. Figure 8 shows the structure of the defect in different charge states as well as the location of excess charges. In the +5 charge state, the interstitial coordinates six oxygen atoms. Five of these are shared with neighboring vanadium atoms, while one is found to dissociate from its previous host, as shown in Figure 8f. Furthermore, each of the oxygen-sharing neighbors forms bonds to oxygen atoms in adjacent layers, with the vanadium to the left and right of the defect in Figure 8f coordinating to five oxygen atoms each. An excess electron is found to localize onto the defect, elongating the V−O bond to one of its shared oxygen atoms. This also breaks the interlayer V−O−V bond between two vanadium atoms (left of the interstitial in Figure 8e). Localization onto the vanadium atom above the interstitial in Figure 8d occurs upon the addition of a second electron, shifting it ∼0.1 Å closer to the defect. A third electron localizes onto the vanadium to the right of the defect in Figure 8c, slightly perturbing its V−O bonds. A fourth electron localizes onto the interstitial itself, which now traps two electrons, elongating the V$_i$−O bonds by an average of ∼0.06 Å. Finally, a fifth electron localizes onto the vanadium atom to the left of the interstitial in Figure 8a, elongating its V−O bonds by an average of ∼0.08 Å.

Interstitial Oxygen. The oxygen interstitial acts as an electron acceptor, donating two excess holes to the lattice at neutral charge. Its structure and charge localization in different charge states are shown in Figure 9. In the absence of excess charges, that is, in the −2 charge state, the interstitial forms V−O bonds with the vanadium atoms of two neighboring VO$_4$ lying in different planes, forming a bridge as seen in Figure 9a. This distorts the unshared V−O bonds: three of them are elongated while one is reduced with respect to the bulk value of ∼1.7 Å. The vanadium atoms are displaced by 0.15 and 0.3 Å toward the interstitial. The V−O$_i$ bond lengths are both ∼2 Å. Charge localization onto the interstitial and another nearby oxygen atom occurs upon the addition of a hole. The V−O bond lengths to the host vanadium are 1.86 and 1.93 Å for these oxygen atoms, and the O−O distance between the two is 2.01 Å. Additionally, the bond from the interstitial to the other VO$_4$ is elongated to 2.16 Å. A second excess hole localizes onto the two hole-trapping oxygen atoms, forming a dimer with an O−O distance of 1.45 Å, similar to that of the O$_2^{2-}$ species.
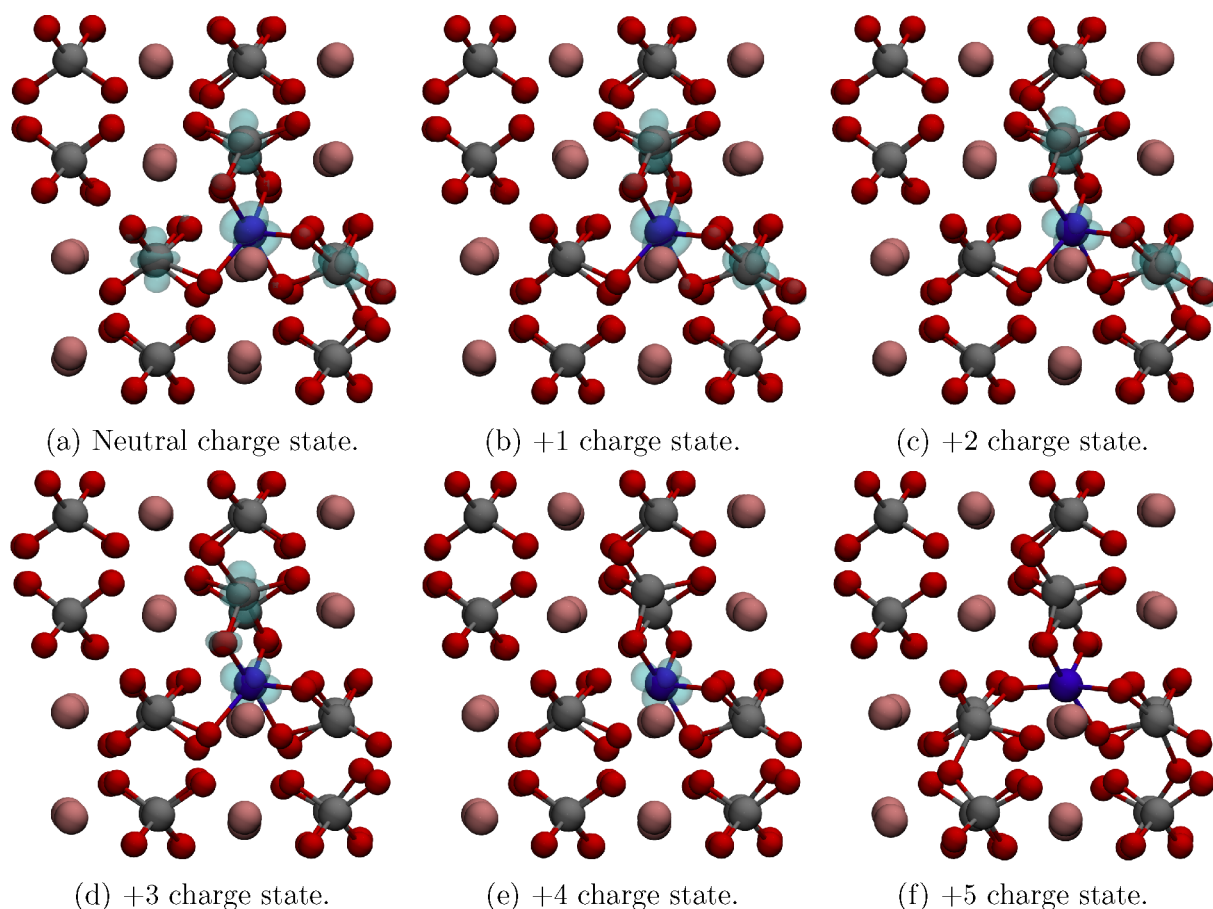
(a) Neutral charge state.   (b) +1 charge state.   (c) +2 charge state.

(d) +3 charge state.   (e) +4 charge state.   (f) +5 charge state.

Figure 8. Lowest-energy configurations for interstitial vanadium. The defect is highlighted in blue. Isosurfaces represent the square modulus of orbitals associated with localized electrons and are shown at 5% of their maximum values.

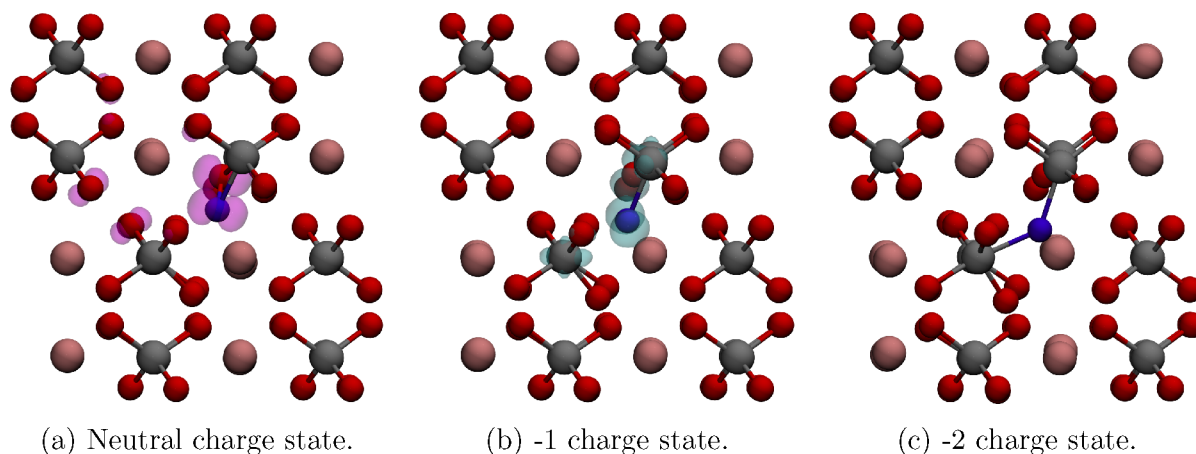(a) Neutral charge state.   (b) -1 charge state.   (c) -2 charge state.

Figure 9. Lowest-energy configurations for interstitial oxygen. The defect is highlighted in blue. Isosurfaces represent the square modulus of orbitals associated with localized charges and are shown at 5% of their maximum values. Holes are shown in cyan, and electron states related to dimer formation are shown in magenta.

As previously observed for cation vacancies, the hole state associated with dimer formation is impossible to isolate. Therefore, Figure 9a shows the highest-lying localized electron state associated with the formation of the dimer for illustrative purposes.

Bismuth Antisite. Replacing a vanadium atom with a bismuth atom, thus creating a bismuth antisite (Bi_V), retains the tetrahedral structure of oxygen atoms surrounding the central cation. The defect is an electron acceptor, yielding two

excess holes in the neutral charge state. The structure and charge localization in different charge states are shown in Figure 10. In the −2 charge state, the Bi_V−O bond lengths are ~2.2 Å. Charge localization onto the defect and surrounding oxygen atoms occurs upon the insertion of a hole, shortening the Bi_i−O bonds to ~2.1 Å. A second hole localizes in a similar fashion, further shortening the Bi_V−O bonds to ~2 Å.

Vanadium Antisite. The V_{Bi} antisite acts as a donor, contributing two excess electrons to the lattice in the neutral

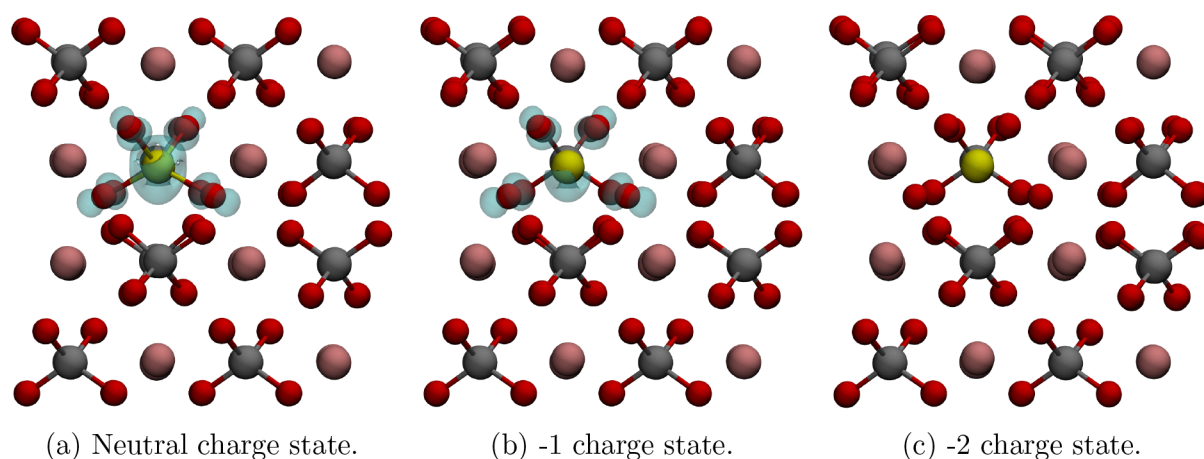(a) Neutral charge state.   (b) -1 charge state.   (c) -2 charge state.

Figure 10. Lowest-energy configurations for the bismuth antisite Bi_V. The defect is highlighted in yellow. Isosurfaces represent the square modulus of orbitals associated with localized holes and are shown at 5% of their maximum values.

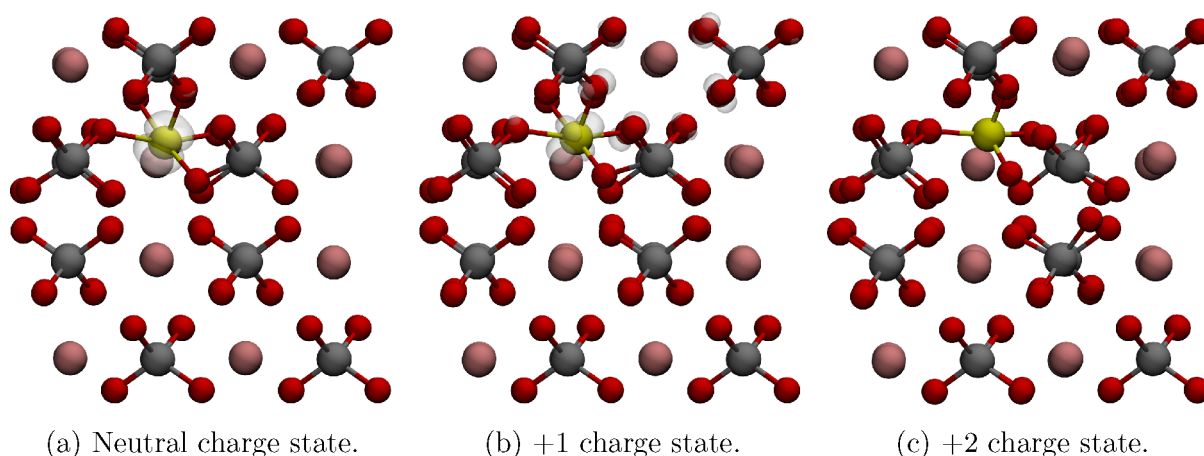(a) Neutral charge state.   (b) +1 charge state.   (c) +2 charge state.

Figure 11. Lowest-energy configurations for the vanadium antisite V_{Bi}. The defect is highlighted in yellow. Isosurfaces represent the square modulus of orbitals associated with localized electrons and are shown at 5% of their maximum values.

charge state. Its introduction results in significant lattice distortions around the defect, with the vanadium forming asymmetric bonds with five nearby oxygen atoms. The local structure resembles that of crystalline V_2O_5, with the oxygen atoms forming a distorted square pyramid. The defect's structure in different charge states, along with the localization of excess charges, is shown in Figure 11. In the absence of excess holes, that is, the +2 charge state, the V_{Bi}−O bond lengths vary between 1.65 and 2.12 Å. Additionally, the oxygen atom with the shortest V_{Bi}−O bond nearly dissociates from its original host vanadium, with the V−O bond elongating to 2.12 Å. To compensate, another oxygen atom from a neighboring VO_4 is brought closer. Adding an excess electron leads to charge localization onto the antisite, causing all but one of the V_{Bi}−O bonds to elongate. A second electron also localizes onto the antisite, further elongating four of the five V_{Bi}−O bonds, while one retains its length.

■ DISCUSSION

We note that the potential energy landscape of the defects we studied is quite complex. Only the lowest-energy, that is, the most stable, configurations are shown above. For instance, an oxygen dimer may form in the presence of the Bi_V antisite, but the dimerless configuration in Figure 10a is more stable, and the precise location of excess charges within the unit cell has a

significant effect on the energetics of the oxygen vacancy.[21,47] The excess charges stemming from the defects under consideration preferentially localize in the vicinity of the defect. Two notable exceptions are the oxygen vacancy and the bismuth interstitial: in the neutral charge state, that is, with all excess charges present in the simulation, one electron localizes far away from the defects. It is important to note that the situation may be different close to the surface, though.

An important observation we make is that the formation of oxygen dimers is favorable in the presence of cation vacancies and oxygen interstitials. The oxygen dimerization phenomenon has previously been predicted to occur upon the insertion of excess holes in $BiVO_4$,[32] TiO_2,[48] and $SrTiO_3$[49] as well as other transition-metal oxides when subjected to extrinsic doping.[51,52] Ambrosio and Wiktor found that the presence of such dimers at the surface of bismuth vanadate leads to a more favorable energy alignment to the redox level associated with oxidation of hydroxyl ions, a crucial step of the water-splitting reaction, and stabilizes the surface in alkaline conditions.[32] While the effect of the defects in the vicinity of the dimer remains to be seen, treating $BiVO_4$ to favor the formation of cation vacancies or oxygen interstitials and, thereby, oxygen dimer formation could be a new avenue for improving the PEC efficiency and stability of the material.

As mentioned in the Introduction, two studies similar to ours have been previously published. Yin et al.[22] studied the native defects of bismuth vanadate using a semilocal exchange-correlation functional, while Zhang et al.[23] additionally performed total energy calculations using DFT+U and hybrid DFT based on geometries optimized using a semilocal functional. While their formation energy plots exhibit superficial agreement with those in Figure 2, such as the Fermi level being pinned by oxygen and bismuth vacancies, there are also important discrepancies. In particular, the formation energy of defect charge states where charge localization takes place is significantly lower in our work. This is to be expected, however, since neither of those studies were able to capture this phenomenon.

Another difference is related to the pinning of Fermi levels and the type of majority charge carriers. Monoclinic $BiVO_4$ is generally considered to be an n-type semiconductor, though there are examples of p-type tetragonal zircon $BiVO_4$ being synthesized without extrinsic doping in the literature.[24,25] Wang et al. attribute the p-type conductivity to bismuth vacancies and oxygen interstitials,[24] which we predict should be the dominant electron acceptor defects at conditions favoring p-type conductivity. The scarcity of examples of undoped p-type monoclinic scheelite $BiVO_4$ in the literature suggests that it is difficult to synthesize, in good agreement with our results. At oxygen-rich conditions, that is, point B of Figure 1, the Fermi level is pinned at ∼0.15 eV below the band gap middle. Adjusting the chemical potentials along the $\mu_O = 0$ line to the vanadium-rich/bismuth-poor stability limit shifts the pinning level to ∼0.23 eV below the band gap middle. Producing p-type $BiVO_4$ thus requires very precise control of synthesis conditions and should result in a sample with poor conductivity. This is in stark contrast to the results of Yin et al. and Zhang et al., who predict Fermi levels pinned much closer to the valence band maximum. Their findings imply that p-type conductivity should be achievable over a larger range of conditions and with high conductivity, a result that does not agree with the available experimental literature. Therefore, charge localization must be taken into account during geometry optimization for even qualitatively correct results.

CONCLUSIONS

In conclusion, we have studied the stability and structure of the native defects in the monoclinic scheelite phase of bismuth vanadate using hybrid density functional theory. We began by investigating the stability of these defects under realistic growth conditions. On the basis of Fermi-level pinning, our results indicate that intrinsic p-type conductivity is very difficult to achieve in the material, in agreement with experimental literature. We then perform a detailed analysis of the local chemical environment around the defects and find that charge localization may have a profound effect on the defect physics. In particular, oxygen dimers may form close to cation vacancies and oxygen interstitials, mediated by the localization of two holes onto two oxygen atoms. Furthermore, we find that one or two additional holes may localize onto these dimers, shortening the O–O bonds to values close to those of the O_2^{1-} and O_2 species, respectively. The presence of these dimers has previously been predicted to have a favorable effect on the water-splitting reaction. Our results thus suggest that treating the material to favor the formation of dimer-forming acceptor defects is a potential new avenue for improving the efficiency of $BiVO_4$ photoanodes. This scheme could be useful for other

complex transition-metal oxides as well, though studies need to be conducted to elucidate whether the trends we observe are general or not.

ASSOCIATED CONTENT

ⓈℹI Supporting Information

The Supporting Information is available free of charge at https://pubs.acs.org/doi/10.1021/acs.jpcc.1c09990.

     Unit cell definitions for chemical potential reference calculations (PDF)

AUTHOR INFORMATION

Corresponding Author

Julia Wiktor − *Department of Physics, Chalmers University of Technology, SE-412 96 Gothenburg, Sweden;* ⓞ orcid.org/0000-0003-3395-1104; Email: julia.wiktor@chalmers.se

Authors

Nicklas Österbacka − *Department of Physics, Chalmers University of Technology, SE-412 96 Gothenburg, Sweden;* ⓞ orcid.org/0000-0002-6043-4607

Francesco Ambrosio − *Computational Laboratory for Hybrid/Organic Photovoltaics, Istituto CNR di Scienze e Tecnologie Chimiche "Giulio Natta", 06123 Perugia, Italy; CNST@Polimi, Istituto Italiano di Tecnologia, 20133 Milano, Italy; Dipartimento di Chimica e Biologia "A. Zambelli", Universitá di Salerno, I-84084 Fisciano, Salerno, Italy;* ⓞ orcid.org/0000-0002-6388-9586

Complete contact information is available at:
https://pubs.acs.org/10.1021/acs.jpcc.1c09990

Notes

The authors declare no competing financial interest.

REFERENCES

(1) Tachibana, Y.; Vayssieres, L.; Durrant, J. R. Artificial Photosynthesis for Solar Water-Splitting. *Nat. Photonics* **2012**, *6*, 511−518.

(2) Yao, T.; An, X.; Han, H.; Chen, J. Q.; Li, C. Photoelectrocatalytic Materials for Solar Water Splitting. *Adv. Energy Mater.* **2018**, *8*, 1800210.

(3) Jiang, C.; Moniz, S. J. A.; Wang, A.; Zhang, T.; Tang, J. Photoelectrochemical Devices for Solar Water Splitting − Materials and Challenges. *Chem. Soc. Rev.* **2017**, *46*, 4645−4660.

(4) Chu, S.; Li, W.; Yan, Y.; Hamann, T.; Shih, I.; Wang, D.; Mi, Z. Roadmap on Solar Water Splitting: Current Status and Future Prospects. *Nano Futures* **2017**, *1*, No. 022001.

(5) Park, Y.; McDonald, K. J.; Choi, K.-S. Progress in Bismuth Vanadate Photoanodes for Use in Solar Water Oxidation. *Chem. Soc. Rev.* **2013**, *42*, 2321−2337.

(6) Sharp, I. D.; Cooper, J. K.; Toma, F. M.; Buonsanti, R. Bismuth Vanadate as a Platform for Accelerating Discovery and Development of Complex Transition-Metal Oxide Photoanodes. *ACS Energy Lett.* **2017**, *2*, 139−150.

(7) Yu, J.; Kudo, A. Effects of Structural Variation on the Photocatalytic Performance of Hydrothermally Synthesized $BiVO_4$. *Adv. Funct. Mater.* **2006**, *16*, 2163−2169.

(8) Zhao, Y.; Li, R.; Mu, L.; Li, C. Significance of Crystal Morphology Controlling in Semiconductor-Based Photocatalysis: A Case Study on BiVO$_4$ Photocatalyst. *Cryst. Growth Des.* **2017**, *17*, 2923−2928.

(9) Ye, H.; Lee, J.; Jang, J. S.; Bard, A. J. Rapid Screening of BiVO$_4$-Based Photocatalysts by Scanning Electrochemical Microscopy (SECM) and Studies of Their Photoelectrochemical Properties. *J. Phys. Chem. C* **2010**, *114*, 13322−13328.

(10) Zhang, B.; Zhang, H.; Wang, Z.; Zhang, X.; Qin, X.; Dai, Y.; Liu, Y.; Wang, P.; Li, Y.; Huang, B. Doping Strategy to Promote the Charge Separation in BiVO$_4$ Photoanodes. *Appl. Catal., B* **2017**, *211*, 258−265.

(11) Kim, T. W.; Choi, K.-S. Nanoporous BiVO$_4$ Photoanodes with Dual-Layer Oxygen Evolution Catalysts for Solar Water Splitting. *Science* **2014**, *343*, 990−994.

(12) Palaniselvam, T.; Shi, L.; Mettela, G.; Anjum, D. H.; Li, R.; Katuri, K. P.; Saikaly, P. E.; Wang, P. Vastly Enhanced BiVO$_4$ Photocatalytic OER Performance by NiCoO$_2$ as Cocatalyst. *Adv. Mater. Interfaces* **2017**, *4*, 1700540.

(13) Trześniewski, B. J.; Smith, W. A. Photocharged BiVO$_4$ Photoanodes for Improved Solar Water Splitting. *J. Mater. Chem. A* **2016**, *4*, 2919−2926.

(14) Lamm, B.; Trześniewski, B. J.; Döscher, H.; Smith, W. A.; Stefik, M. Emerging Postsynthetic Improvements of BiVO$_4$ Photoanodes for Solar Water Splitting. *ACS Energy Lett.* **2018**, *3*, 112−124.

(15) Zhang, W.; Song, L.; Cen, J.; Liu, M. Mechanistic Insights into Defect-Assisted Carrier Transport in Bismuth Vanadate Photoanodes. *J. Phys. Chem. C* **2019**, *123*, 20730−20736.

(16) Wu, J.-M.; Chen, Y.; Pan, L.; Wang, P.; Cui, Y.; Kong, D.; Wang, L.; Zhang, X.; Zou, J.-J. Multi-Layer Monoclinic BiVO$_4$ with Oxygen Vacancies and V^{4+} Species for Highly Efficient Visible-Light Photoelectrochemical Applications. *Appl. Catal., B* **2018**, *221*, 187−195.

(17) Wang, S.; Chen, P.; Bai, Y.; Yun, J.-H.; Liu, G.; Wang, L. New BiVO$_4$ Dual Photoanodes with Enriched Oxygen Vacancies for Efficient Solar-Driven Water Splitting. *Adv. Mater.* **2018**, *30*, 1800486.

(18) Qiu, W.; Xiao, S.; Ke, J.; Wang, Z.; Tang, S.; Zhang, K.; Qian, W.; Huang, Y.; Huang, D.; Tong, Y.; Yang, S. Freeing the Polarons to Facilitate Charge Transport in BiVO$_4$ from Oxygen Vacancies with an Oxidative 2D Precursor. *Angew. Chem.* **2019**, *131*, 19263−19271.

(19) Hegner, F. S.; Forrer, D.; Galán-Mascarós, J. R.; López, N.; Selloni, A. Versatile Nature of Oxygen Vacancies in Bismuth Vanadate Bulk and (001) Surface. *J. Phys. Chem. Lett.* **2019**, *10*, 6672−6678.

(20) Wang, W.; Strohbeen, P. J.; Lee, D.; Zhou, C.; Kawasaki, J. K.; Choi, K.-S.; Liu, M.; Galli, G. The Role of Surface Oxygen Vacancies in BiVO$_4$. *Chem. Mater.* **2020**, *32*, 2899−2909.

(21) Österbacka, N.; Wiktor, J. Influence of Oxygen Vacancies on the Structure of BiVO$_4$. *J. Phys. Chem. C* **2021**, *125*, 1200−1207.

(22) Yin, W.-J.; Wei, S.-H.; Al-Jassim, M. M.; Turner, J.; Yan, Y. Doping Properties of Monoclinic BiVO$_4$ Studied by First-Principles Density-Functional Theory. *Phys. Rev. B* **2011**, *83*, 155102.

(23) Zhang, J.; Chen, X.; Deng, M.; Shen, H.; Li, H.; Ding, J.-w. Effects of Native Defects and Cerium Impurity on Monoclinic BiVO$_4$ Photocatalyst by PBE+U Calculations. *Phys. Chem. Chem. Phys.* **2020**, *22*, 25297.

(24) Wang, J.; Song, Y.; Hu, J.; Li, Y.; Wang, Z.; Yang, P.; Wang, G.; Ma, Q.; Che, Q.; Dai, Y.; Huang, B. Photocatalytic Hydrogen Evolution on P-Type Tetragonal Zircon BiVO$_4$. *Appl. Catal., B* **2019**, *251*, 94−101.

(25) Bai, Y.; Lu, J.; Bai, H.; Fang, Z.; Wang, F.; Liu, Y.; Sun, D.; Luo, B.; Fan, W.; Shi, W. Understanding the Key Role of Vanadium in P-Type BiVO$_4$ for Photoelectrochemical N$_2$ Fixation. *Chem. Eng. J.* **2021**, *414*, 128773.

(26) Cooper, J. K.; Scott, S. B.; Ling, Y.; Yang, J.; Hao, S.; Li, Y.; Toma, F. M.; Stutzmann, M.; Lakshmi, K. V.; Sharp, I. D. Role of Hydrogen in Defining the N-Type Character of BiVO$_4$ Photoanodes. *Chem. Mater.* **2016**, *28*, 5761−5771.

(27) Kweon, K. E.; Hwang, G. S. Surface Structure and Hole Localization in Bismuth Vanadate: A First Principles Study. *Appl. Phys. Lett.* **2013**, *103*, 131603.

(28) Liu, T.; Zhou, X.; Dupuis, M.; Li, C. The Nature of Photogenerated Charge Separation Among Different Crystal Facets of BiVO$_4$ Studied by Density Functional Theory. *Phys. Chem. Chem. Phys.* **2015**, *17*, 23503−23510.

(29) Kweon, K. E.; Hwang, G. S.; Kim, J.; Kim, S.; Kim, S. Electron Small Polarons and Their Transport in Bismuth Vanadate: A First Principles Study. *Phys. Chem. Chem. Phys.* **2015**, *17*, 256−260.

(30) Wiktor, J.; Ambrosio, F.; Pasquarello, A. Role of Polarons in Water Splitting: The Case of BiVO$_4$. *ACS Energy Lett.* **2018**, *3*, 1693−1697.

(31) Wiktor, J.; Pasquarello, A. Electron and Hole Polarons at the BiVO$_4$−Water Interface. *ACS Appl. Mater. Interfaces* **2019**, *11*, 18423−18426.

(32) Ambrosio, F.; Wiktor, J. Strong Hole Trapping Due to Oxygen Dimers in BiVO$_4$: Effect on the Water Oxidation Reaction. *J. Phys. Chem. Lett.* **2019**, *10*, 7113−7118.

(33) Pacchioni, G.; Frigoli, F.; Ricci, D.; Weil, J. A. Theoretical Description of Hole Localization in a Quartz Al Center: The Importance of Exact Electron Exchange. *Phys. Rev. B* **2000**, *63*, No. 054102.

(34) Lægsgaard, J.; Stokbro, K. Hole Trapping at Al Impurities in Silica: A Challenge for Density Functional Theories. *Phys. Rev. Lett.* **2001**, *86*, 2834−2837.

(35) Erhart, P.; Klein, A.; Åberg, D.; Sadigh, B. Efficacy of the DFT + *U* Formalism for Modeling Hole Polarons in Perovskite Oxides. *Phys. Rev. B* **2014**, *90*, No. 035204.

(36) Miceli, G.; Chen, W.; Reshetnyak, I.; Pasquarello, A. Nonempirical Hybrid Functionals for Band Gaps and Polaronic Distortions in Solids. *Phys. Rev. B* **2018**, *97*, 121112.

(37) Kühne, T. D.; Iannuzzi, M.; Del Ben, M.; Rybkin, V. V.; Seewald, P.; Stein, F.; Laino, T.; Khaliullin, R. Z.; Schütt, O.; Schiffmann, F.; Golze, D.; Wilhelm, J.; Chulkov, S.; Bani-Hashemian, M. H.; Weber, V.; Borštnik, U.; Taillefumier, M.; Jakobovits, A. S.; Lazzaro, A.; Pabst, H.; Müller, T.; Schade, R.; Guidon, M.; Andermatt, S.; Holmberg, N.; Schenter, G. K.; Hehn, A.; Bussy, A.; Belleflamme, F.; Tabacchi, G.; Glöß, A.; Lass, M.; Bethune, I.; Mundy, C. J.; Plessl, C.; Watkins, M.; VandeVondele, J.; Krack, M.; Hutter, J. CP2K: An Electronic Structure and Molecular Dynamics Software Package - Quickstep: Efficient and Accurate Electronic Structure Calculations. *J. Chem. Phys.* **2020**, *152*, 194103.

(38) Goedecker, S.; Teter, M.; Hutter, J. Separable Dual-Space Gaussian Pseudopotentials. *Phys. Rev. B* **1996**, *54*, 1703−1710.

(39) VandeVondele, J.; Hutter, J. Gaussian Basis Sets for Accurate Calculations on Molecular Systems in Gas and Condensed Phases. *J. Chem. Phys.* **2007**, *127*, 114105.

(40) Perdew, J. P.; Ernzerhof, M.; Burke, K. Rationale for Mixing Exact Exchange with Density Functional Approximations. *J. Chem. Phys.* **1996**, *105*, 9982−9985.

(41) Guidon, M.; Hutter, J.; VandeVondele, J. Robust Periodic Hartree-Fock Exchange for Large-Scale Simulations Using Gaussian Basis Sets. *J. Chem. Theory Comput.* **2009**, *5*, 3010−3021.

(42) Guidon, M.; Hutter, J.; VandeVondele, J. Auxiliary Density Matrix Methods for Hartree-Fock Exchange Calculations. *J. Chem. Theory Comput.* **2010**, *6*, 2348−2364.

(43) Sleight, A.W.; Chen, H.-Y.; Ferretti, A.; Cox, D.E. Crystal Growth and Structure of BiVO$_4$. *Mater. Res. Bull.* **1979**, *14*, 1571−1581.

(44) Freysoldt, C.; Grabowski, B.; Hickel, T.; Neugebauer, J.; Kresse, G.; Janotti, A.; Van de Walle, C. G. First-Principles Calculations for Point Defects in Solids. *Rev. Mod. Phys.* **2014**, *86*, 253−305.

(45) Freysoldt, C.; Neugebauer, J.; Van de Walle, C. G. Fully Ab Initio Finite-Size Corrections for Charged-Defect Supercell Calculations. *Phys. Rev. Lett.* **2009**, *102*, No. 016402.

(46) Ambrosio, F.; Wiktor, J.; Pasquarello, A. pH-Dependent Catalytic Reaction Pathway for Water Splitting at the BiVO$_4$−Water

Interface from the Band Alignment. *ACS Energy Lett.* **2018**, *3*, 829−834.

(47) Seo, H.; Ping, Y.; Galli, G. Role of Point Defects in Enhancing the Conductivity of $BiVO_4$. *Chem. Mater.* **2018**, *30*, 7793−7802.

(48) Chen, S.; Wang, L.-W. Double-Hole-Induced Oxygen Dimerization in Transition Metal Oxides. *Phys. Rev. B* **2014**, *89*, No. 014109.

(49) Chen, H.; Umezawa, N. Hole Localization, Migration, and the Formation of Peroxide Anion in Perovskite $SrTiO_3$. *Phys. Rev. B* **2014**, *90*, No. 035202.

(50) Guo, Z.; Ambrosio, F.; Pasquarello, A. Oxygen Defects in Amorphous Al_2O_3: A Hybrid Functional Study. *Appl. Phys. Lett.* **2016**, *109*, No. 062903.

(51) Koch, D.; Manzhos, S. Interstitial versus Substitutional Metal Insertion in V_2O_5 as Post-Lithium Ion Battery Cathode: A Comparative GGA/GGA + U Study with Localized Bases. *MRS Commun.* **2020**, *10*, 259−264.

(52) Koch, D.; Manzhos, S. Can Doping of Transition Metal Oxide Cathode Materials Increase Achievable Voltages with Multivalent Metals? *Int. J. Quantum Chem.* **2021**, *121*, No. e26439.